Scilight

Regenerative Medicine and Dentistry
https://www.sciltp.com/journals/rmd

Article

Graphene Oxide/Chitosan/Calcium Silicate Aerogels for Hemostasis and Infectious Wound Healing

Jianmin Xue [1,2,†], Yi Zheng [1,2,†], Zhibo Yang [1,2], Jinzhou Huang [1,2], Wenping Ma [1,2], Zhiguang Huan [1,2], Yufang Zhu [1,2,*] and Chengtie Wu [1,2,*]

[1] State Key Laboratory of High Performance Ceramics and Superfine Microstruture, Shanghai Institute of Ceramics, Chinese Academy of Sciences, Shanghai 200050, China
[2] Center of Materials Science and Optoelectronics Engineering, University of Chinese Academy of Sciences, Beijing 100049, China
* Correspondence: zjf2412@163.com (Y.Z.); chengtiewu@mail.sic.ac.cn (C.W.)
† These authors contributed equally to this work.

How To Cite: Xue, J.; Zheng, Y.; Yang, Z.; et al. Graphene Oxide/Chitosan/Calcium Silicate Aerogels for Hemostasis and Infectious Wound Healing. *Regenerative Medicine and Dentistry* **2025**, *2*(2), 8. https://doi.org/10.53941/100008.

Received: 1 April 2025
Revised: 9 June 2025
Accepted: 13 June 2025
Published: 18 June 2025

Abstract: Uncontrolled hemorrhage is still the great obstacle for saving life during accident or surgery. In addition, hemostatic materials integrating with both rapid hemostasis and wound healing functions are of great significance in clinic. In this work, we successfully developed graphene oxide/chitosan/calcium silicate aerogels with good hemostasis, anti-bacteria and wound healing abilities. The porous lamellar structure with interconnected channels were constructed in aerogels, which enabled the rapid liquid-absorbing capacity and certain elasticity. Moreover, the graphene oxide/chitosan/calcium silicate aerogels exhibited good blood clotting ability in vitro and fast stop bleeding effect in vivo, far exceeding the hemostatic effect of gauze. Additionally, the graphene oxide/chitosan/calcium silicate aerogels could not only accumulate blood cells to promote primary hemostasis, but also activate the intrinsic pathway of coagulation during second hemostasis owing to the graphene oxide and bioactive components (Ca and Si ions). For the repairing of infectious skin wounds, such aerogels could inhibit inflammation after photothermal therapy at early stage and achieve high healing quality after 14 days. These multifunctional aerogels are promising biomaterials for uncontrolled hemorrhage and subsequently tissue skin tissue healing of emergency trauma.

Keywords: graphene oxide; hemostatic aerogels; anti-bacteria; wound healing

1. Introduction

Serious trauma in the accident or surgical process typically accompanied with massive hemorrhage of intrathoracic organs or vasculature. The incontrollable bleeding is one of the commonest causes of death in the pre-hospital treatment [1,2]. However, traditional tourniquets or gauze cannot afford the requirements of rapid hemostasis. Therefore, in the past decades, various types of materials, such as hemostatic sponges/foams [3–9], hydrogel sealants [10–13], hemostatic powders [14–17], were developed to fulfill the requirements of traumatic bleeding. Among these hemostatic materials, sponges/foams possessed high porous structure and good liquid-absorbing ability, which could facilitate coagulation by concentrating blood cells, platelets and blood proteins [1,2,18]. Moreover, the hemostatic sponges/foams are lightweight to carry and store as well as ease of use for non-trained peoples [2]. Therefore, some common hemostatic polymers, such as chitosan and gelatin, were made into sponges/foams for hemorrhage control [7,19].

Although hemostatic sponges/foams show great potential in commercial application, they still have many adversities that should be overcome in future. For example, most of sponges/foams were fabricated by directly lyophilization or foaming process, which would lead to the random porous structure [20,21]. The high tortuosity

of random porous structure would increase the liquid flow resistance and reduce the blood-absorbing rate [22]. Besides, hemostasis was typically accompanied by skin tissue damage. In addition, the damaged tissue sites also easily infected by bacteria under the complex and uncleanly accident environments, which would delay wound healing [1,2,23]. However, to date, few hemostatic sponges could meet once-and-for-all treatment, including both hemorrhage control, anti-infection and wound healing.

Recently, carbon-based sponges have gained great attention in application of rapid hemostasis. Previous studies reported that graphene oxide (GO)-based sponges were better to promote the liquid-absorbing ability and induce the platelets aggregation [6,19,20,24]. Based on the photothermal effect of graphene oxide or carbon nanotube, carbon-based materials showed good anti-bacterial effect in wound healing [24–26]. On the other hand, inorganic bioactive components, such as hydroxyapatite or bioactive glass, have already verified the ideal tissue repairing effect due to the released bioactive ions, which were also showed potential in hemostatic materials [27]. Moreover, by constructing the ordered and interconnected channels, the biomaterials could improve blood-absorbing capability and hemostasis effect [22,28,29]. Therefore, through the combination of the specific composition and microstructure, it is expected to obtain biomaterials with rapid hemostasis, anti-infection and wound healing ability.

Herein, in order to overcome the shortcomings of the existing hemostatic materials, we successfully fabricated graphene oxide/chitosan/calcium silicate aerogels with multiple functions including good hemostasis, anti-bacteria and wound healing abilities. The repaid liquid absorbing ability and high elasticity were achieved due to the construction of oriented porous structure. The rapid hemostasis and hemostatic mechanisms were systematically accessed by determining the blood clotting index (BCI), partial thromboplatin time (PTT), red blood cell (RBC) adhesion and in vivo hemostasis time. The anti-bacterial and accelerated wound healing effect of aerogels were also observed from in vivo infectious skin wound healing assay.

2. Materials and Methods

2.1. Chemical and Reagents

The $Ca(NO_3)_2$•$4H_2O$, Na_2SiO_3•$9H_2O$, chitosan and acetic acid were purchased from Sinopharm Chemical Reagent Co., Ltd., Shanghai, China. The graphite oxide was purchased from Shanghai Haoye Electronic Technology Co., Ltd., Shanghai, China The single layer graphene oxide was purchased from Suzhou Tanfeng Graphene Technology Co., Ltd., Suzhou, China.

2.2. Fabrication of Graphene Oxide/Chitosan/Amorphous Calcium Silicate (GC-CS) Aerogels

5 g of chitosan and 10 mL of acetic acid were added into 990 mL of deionized water to obtain chitosan solution. GO suspension (1 mg/mL) was obtained by adding graphite oxide powders into deionized water and ultrasonicated by ultrasonic instrument. The ultrasonic frequency and ultrasonic time were 53 kHz and 4 h, respectively. The GO suspension and chitosan (CTS) solution were mixed by stirring. Then, Na_2SiO_3•$9H_2O$ and $Ca(NO_3)_2$•$4H_2O$ were sequentially added into mixed solution. Subsequently, the pH of solution was adjusted to 10 approximately with NH_3•H_2O. After reaction for 2 h, the mixed solution was filtered to obtain the GC-CS composite green body. Finally, the GC-CS aerogels were prepared by freeze-drying of green body. The GC-CS aerogels with GO contents of 30 wt.%, 50 wt.% and 70 wt.% were named as GC-CS-I, GC-CS-II and GC-CS-III, respectively (the theoretical content of calcium silicate was fixed at 20%). The GC-I aerogels without bioactive component were also fabricated as control group. During the preparation process of GC-I, the GO suspension and chitosan solution were mixed, filtrated and freeze-dried to obtain final GC-I aerogels.

2.3. Fabrication of Graphene Oxide/Chitosan/Calcium Silicate Nanofiber (GC-nfCS) Aerogels

100 mL of Na_2SiO_3•$9H_2O$ aqueous solution (0.4 mol/L) was mixed with 100 mL of $Ca(NO_3)_2$•$4H_2O$ aqueous solution (0.4 mol/L) and stirred continuously for 1 h to form a uniform white suspension. The suspension was hydrothermally reacted at 200 ℃ for 24 h. Then, the suspension was filtered and washed three times with absolute ethanol and deionized water to obtain uniform calcium silicate (CS) nanofiber.

Three GC-nfCS aerogels, named as GC-nfCS-I, GC-nfCS-II and GC-nfCS-III, respectively, were fabricated by freeze-drying method. The constituent contents of each aerogel were listed in Table S1. Taken GC-nfCS-II as example, the fabrication process was conducted as follows. 1.5 mL of acetic acid was added into 148.5 mL of deionized water to obtain 1% acetic acid solution. The 4.5 g of CTS powders were dissolved into acetic acid solution to obtain chitosan solution (30 mg/mL). 70 mg of GO and 10 mg of CS nanowires were added in deionized water and sonicated to obtain GO/CS suspension. Then, 1 mL of chitosan solution (30 mg/mL) was mixed with

GO/CS suspension and stirred for 24 h to obtain homogeneous GC-nfCS suspension. The GC-nfCS suspension was poured into the silicone mold and frozen at −80 ℃ for 30 min. After that, the frozen green body was freeze-dried and then processed at 60 ℃ oven for 24 h to obtain the final GC-nfCS aerogels. In addition, the GC-II aerogels without CS nanowires were fabricated as control group. The preparation process of GC-II was similar to that of GC-nfCS aerogel but without addition of CS nanowires.

2.4. Characterization of Physicochemical Properties

The microstructures and elements distribution of different aerogels were characterized by field emission scanning electron microscope (SEM, SU8220, Hitachi, Japan) accompanying with energy dispersive spectrometer (EDS). The X-ray diffraction (XRD) patterns of different aerogels were determined by X-ray diffractometer (D8 ADVANCE, Bruker, Germany). Fourier transform infrared (FTIR) spectra of different aerogels were characterized by FTIR spectroscopy (Bruker Tensor 27, Bruker, Germany). The cyclic compression performance of aerogels was tested using a static mechanical testing machine (INSTRON 5566, Instron, UK). In vitro photothermal performance of aerogels was determined by thermal imaging system (PM100D, Thorlabs GmbH, Bergkirchen, Germany) under laser irradiation (808 nm, 0.30 W, 5 min).

To determine rapid liquid absorption capacity, different aerogels were immersed into deionized water within 5 s. The rapid liquid absorption capacity was calculated according to the following equation:

$$\text{Water absorption capacity} = \frac{W_1 - W_0}{W_0} \times 100\%$$

where W_0 and W_1 represent the mass of aerogels before and after immersing into deionized water, respectively. The number of samples in each group of liquid absorption experiment was 3.

For the characterization of zeta potentials, the different aerogels were milled to powders and then dispersed in deionized water by using ultrasonic disperser. The zeta potential of suspension of aerogels was characterized by using zeta potentiometer (90Plus PALS, Brookhaven, NY, USA). The number of samples in each group of zeta potential was 3.

2.5. In Vitro Coagulation Ability

The aerogels (5 mm ×5 mm ×10 mm) were put into centrifuge tube and warmed up at 37 ℃ in advance. 100 μL of fresh anticoagulated rat blood were dropped on aerogels and then added 10 μL of $CaCl_2$ solution (0.2 mol/L). Then, the aerogels were subsequently incubated at 37 ℃ for 1 min and immediately added PBS solution (10 mL) into centrifuge tube. The absence of solution at 540 nm was determined by microplate reader. The blood clotting index (BCI) was calculated according to the following equation:

$$\text{BCI} = \frac{A_x}{A_{\text{positive control}}} \times 100\%$$

where A_x and $A_{\text{positive control}}$ represent the absorbance of material groups and positive control group, respectively. The number of samples in each group of BCI assay was 5.

2.6. Hemolysis Rate

The aerogels were dispersed in PBS to obtain suspension with concentration of 2 mg/mL. Then, 50 μL of red cell enriched solution was added to the suspension and incubated at 37 ℃ for 1 h. The absorbance of aerogel at 540 nm was determined. The in vitro hemolysis rate of the material was calculated according to the following formula:

$$\text{Hemolysis rate} = \frac{A_x - A_{\text{negative control}}}{A_{\text{positive control}} - A_{\text{negative control}}} \times 100\%$$

where A_x represents the absorbance of the red cell enriched solution after adding with aerogels suspension; $A_{\text{negative control}}$ is the absorbance of the red cell enriched solution after adding with PBS; $A_{\text{positive control}}$ is the absorbance of the red cell enriched solution after adding with deionized water group. The number of samples in each group of hemolysis rate assay was 3.

2.7. Cell Adhesion

The fresh citrate-anticoagulated rat blood was added to the aerogel dressing and incubated at 37 ℃ for 30 min. After that, the blood cells were fixed and gradient dehydrated. The adhesion morphology of blood cells was observed by SEM.

2.8. In Vivo Hemostatic Performance

All procedures were approved by the Institutional Animal Care and Use Committee of Nanjing First Hospital, Nanjing Medical University (DWSY-2102163). The in vivo hemostatic performance of aerogels was evaluated by rat liver bleeding model. The liver was punctured 5 times by syringe needle, and then immediately placed on the aerogels to stop the bleeding. The hemostasis time and blood loss amount were recorded after hemostasis. The number of animals in each group of in vivo hemostatic assay was 4.

2.9. In Vivo Infectious Skin Wound Healing Performance

All procedures were approved by the Institutional Animal Care and Use Committee of Nanjing First Hospital, Nanjing Medical University (DWSY-2102163). The wound healing performance of graphene oxide/chitosan/calcium silicate aerogels were evaluated by infectious skin wound model. The BALB/c mice were 8 weeks old. A skin wound with diameter of 8 mm was created on the back of mouse, and dropped with *S. aureus* bacterial suspension (about 10^7 cells/mL) to the wound site. The wound was fixed with dressing for 2 days to ensure the infectious status. During the operation, the animals were inhalational anesthetized with isoflurane. The mice were well fed with adequate food and water under approximately 25 ℃ after the operation. The mice were randomly divided into five groups: Gauze, Gelatin sponge, GC-I, GC-nfCS-II and GC-CS-II. The infectious wounds were covered different materials (8 mm of diameter) and photographed at 0, 4, 7, 10 and 14 days. The skin wound area was determined by ImageJ software. For the groups of GC-I, GC-nfCS-II and GC-CS-II, the mice were performed with photothermal treatment at 0, 1, 2 days. The wavelength of near infrared light is 808 nm. The aerogel-covered wound was irradiated with near infrared light for 10 min and kept temperature at 50–56 ℃. After 14 days, the mice were sacrificed to collect skin tissue for histological analysis. The repairing effect of the skin tissue at the wound was observed by H&E staining and Masson staining. The number of animals in each group of infectious skin wound healing assay was 5.

2.10. Statistical Analysis

The data were expressed as the mean ± standard deviation (SD). One-way ANOVA was applied to evaluate significant difference between two groups. Significant differences: $p < 0.05$ (*), $p < 0.01$(**), and $p < 0.001$(***).

3. Results and Discussion

3.1. Preparation Strategy and Microstructure of Aerogels

As described before, graphene oxide-based sponges/aerogels have developed for promoting the hemostasis in last decade. Chitosan (CTS) is a common biomaterial with good hemostasis due to remarkable abilities about red blood cells aggregation and platelets adhesion [1,30]. Bioactive ions released from bioceramics, such as Ca^{2+} and SiO_3^{2-}, have been demonstrated the promoting effect on osteogenesis and angiogenesis [31,32]. In this work, two types of calcium silicate bioactive components, i.e., amorphous calcium silicate (CS) and calcium silicate hydrate nanofibers (nfCS), were respectively composited with GO and CTS to form aerogels (named as GC-CS and GC-nfCS, respectively) (Figure 1). Furthermore, in order to investigate the effect of different component contents on material properties, three types of GC-CS aerogels with different constituent contents were fabricated and named as GC-CS-I, GC-CS-II and GC-CS-III, respectively. Similarly, three GC-nfCS aerogels with different constituent contents were also fabricated and named as GC-nfCS-I, GC-nfCS-II and GC-nfCS-III, respectively. The constituent contents of each aerogel were listed in Table S1. For the GC-CS aerogels, Ca^{2+} and SiO_3^{2-} were added into GO and CTS solution to in situ synthesis of amorphous calcium silicate. The final GC-CS aerogels were obtained after vacuum filtration and freeze-drying processes. As for GC-nfCS aerogels, the calcium silicate hydrate nanofibers were synthesized through hydrothermal method (Figures S1 and S2) and then mixed with GO and CTS to fabricate aerogels.

The cross-section morphologies of different aerogels were characterized by scanning electron microscope (SEM) to confirm the existence of oriented porous structure. As shown in Figure 2A, three types of GC-CS aerogels successfully achieved porous lamellar structure under the function of vacuum filtration-assisted assembly and freeze-drying. The GC-CS aerogels showed better orderly microstructure with the increase of GO content. In addition, as shown in high magnification SEM image, the GC-CS-II aerogels (W_{GO}: W_{CTS}: W_{CS} (wt.%) = 50:30:20) possessed "brick-and-mortar" interlayered nanostructure similar to that of nacre. However, the nacre-like interlayered nanostructure cannot be observed in GC-CS-III aerogels (W_{GO}: W_{CTS}: W_{CS} (wt.%) = 70: 10: 20) due to low content of organic chitosan components. The EDS mapping confirmed the calcium and silicon elements

were successfully incorporated into the GC-CS aerogels (Figure S3). For the GC-nfCS aerogels, it is clearly observed channel-like porous structure inside aerogels even without vacuum filtration-assisted assembly (Figure 2B). Especially, the GC-nfCS-II aerogel (W_{GO}: W_{CTS}: Wnf_{CS} (wt.%) = 70: 30: 10) achieved oriented channel microstructure at multiple length scales. It could be due to single layer GO in GC-nfCS aerogels were more easily directional assembly than GO ultrasonic exfoliated from graphite oxide in GC-CS aerogels. Moreover, compared with GC-CS aerogels, the GC-nfCS aerogel showed higher porosity with large interlayer spacing and possessed little interconnected bridges between lamellar layers, which may affect the mechanical performance of GC-nfCS aerogel. Besides, the aerogels were further characterized by X-ray diffraction (XRD) and Fourier transform infrared spectroscopy (FTIR). XRD patterns of GC-CS-II and GC-nfCS-II aerogels showed sharp diffraction peaks at approximately 11°, which was characteristic peak of GO and reflected interlayer ordering of GO nanosheets (Figure S5A,B) [33]. FTIR spectra showed no clear difference between the GC-I and GC-CS-II aerogels. Same result was also observed in FTIR spectra of GC-II and GC-nfCS-II aerogels (Figure S5C). Taken together, we successfully fabricated two types of graphene oxide/chitosan/calcium silicate aerogels with oriented porous structure.

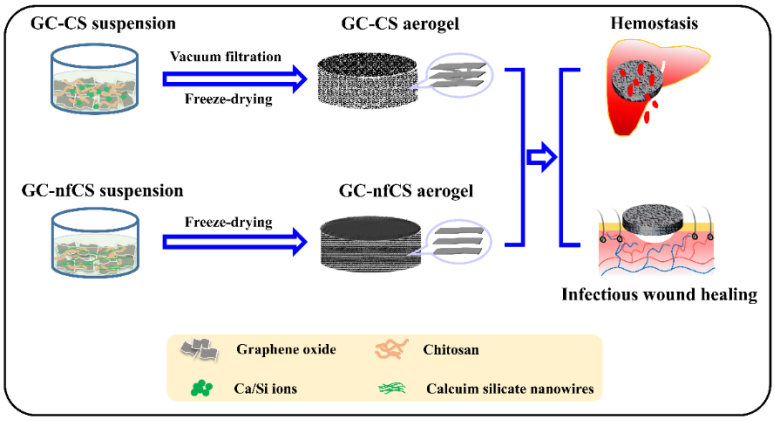

Figure 1. Schematic illustration of the design strategy of GC-CS and GC-nfCS aerogels. Two types of multifunctional graphene oxide/chitosan/calcium silicate aerogels were designed through the combination of the specific composition and microstructure.

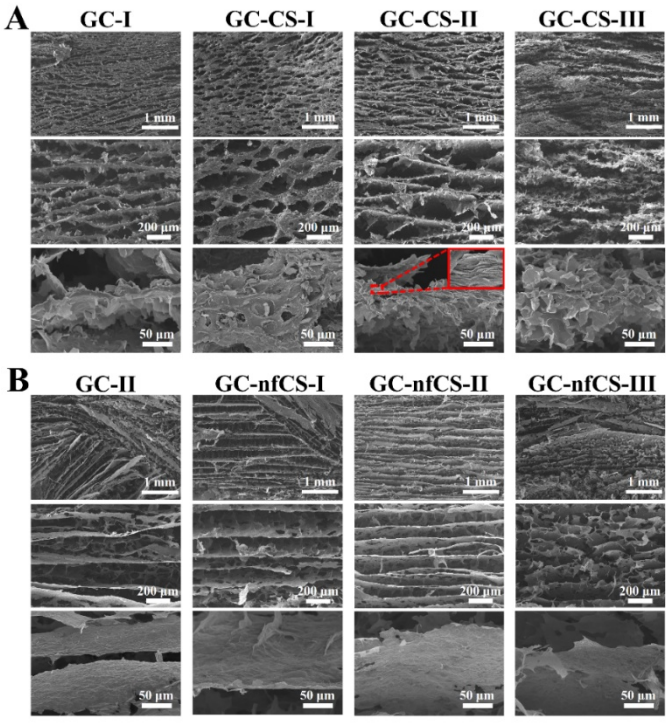

Figure 2. The cross-section morphologies of different aerogels. (**A**) GC-CS aerogels; (**B**) GC-nfCS aerogels. Two types of graphene oxide/bioactive components-based aerogels showed porous microstructure with orderly channels.

3.2. Liquid Absorption Capacity, In Vitro Photothermal Performance, Hemostasis and Hemolysis Ability

The liquid absorption capacity, photothermal performance, blood clotting index (BCI) and hemolysis rate were further investigated to screen out the ideal components of aerogels. The repaid liquid absorption capacity is a vital factor for fast hemorrhage control. One of basic hemostatic mechanism of porous hemostatic materials is to absorb blood and concentrate platelets and coagulation factors as soon as possible. As described before, Yang et al. [22] developed collagen-based foams with parallel channel microstructure, which showed higher liquid absorbing ability and more rapid expansion rate than foams with random microstructure. Considering oriented porous structure of GC-CS and GC-nfCS aerogels, we further investigated rapid liquid absorption capacity by immersion in water within 5 s. The liquid absorption tests showed that both GC-CS and GC-nfCS aerogels could achieve high mass ratio of absorption liquid within 5 s. The weight of water absorbed by GC-CS-II and GC-CS-III aerogels could reach 13.7 times and 16.8 times of their own weight, respectively (Figure 3A). Moreover, the weight of water absorbed by different GC-nfCS aerogels could reach 50 times higher than their own weight (Figure 3B). The better performance of liquid absorption of GC-nfCS aerogels may derived from their higher porosity and more orderly lamellar channel structure without bridges. Overall, the GC-CS and GC-nfCS aerogels possessed superior liquid absorption capacity, which is of great significance for blood absorption and blood cell aggregation in the subsequent hemostasis process.

BCI test was further used to quantitatively evaluate the in vitro hemostatic performance of aerogels. The BCI was determined by measuring the absorbance of unclotted blood at 540 nm of optical density. Hemostatic materials with good blood coagulability result in low BCI values. All of the GC-CS and GC-nfCS aerogels showed low BCI values ranging from 9.5–15.8% (Figure 3C). On the contrary, the BCI values of gauze and gelatin sponge were 37.9% and 25.1%, respectively, which were obviously higher than those GC-CS and GC-nfCS aerogels. As shown in Figure S6, after the blood absorbed by different materials for 1 min, the solutions in the gauze and gelatin sponge groups exhibited obviously red color, indicating that there was still a large amount of unclotted blood. However, all of the GC-CS and GC-nfCS groups obviously possessed more clear solutions due to the better blood coagulation capacity. However, it should be noticed that the GC-nfCS aerogels showed volume shrinkage and lost their shape after absorbing blood (Figure 3D). The volume shrinkage of GC-nfCS aerogels mainly resulted from their high porosity and channel structure without supporting bridges. Although the liquid absorption capacity of GC-CS aerogel was not as high as GC-nfCS aerogel, the GC-CS aerogels could keep shape very well after absorbing blood.

Good hemocompatibility is an essential requirement for biomedical materials. The absorbance test of hemoglobin was applied for determining hemolysis rate of different aerogels. As shown in Figure 3E,F, the hemolysis rate of GC-CS and GC-nfCS aerogels were all lower than 2%, proving the good blood compatibility of these graphene oxide/chitosan/calcium silicate aerogels. In particular, the hemolysis rates of GC-CS-II, GC-nfCS-I and GC-nfCS-II aerogels were 0.53%, 0.38% and 0.55%, respectively, which were greatly meet the requirement of the international standard (5%).

GO-based composites were already widely used in anti-bacteria due to good photothermal effect [20,34−36]. It was reported that the GO-based composites could convert light energy into heat energy and produce local high temperature under near-infrared irradiation, thus destroying the bacterial membrane structure and killing bacteria [35,36]. Therefore, in vitro photothermal performance was also determined. As shown in Figure S7, the temperatures of GC-CS-II and GC-nfCS-II aerogels were rapidly raised above 100 ℃ after 2 min of laser irradiation, indicating the excellent photothermal performance of graphene oxide/chitosan/calcium silicate aerogels. On the contrary, the gauze and gelatin sponge had no obvious temperature change (less than 2 ℃) under same laser irradiation condition.

The above results prove that GC-CS and GC-nfCS aerogels had ideal liquid absorption capacity, in vitro hemostatic, hemolysis capacity and photothermal effect. Considering comprehensive performance of aerogels, GC-CS-II and GC-nfCS-II aerogels were selected as typical ones for further investigation.

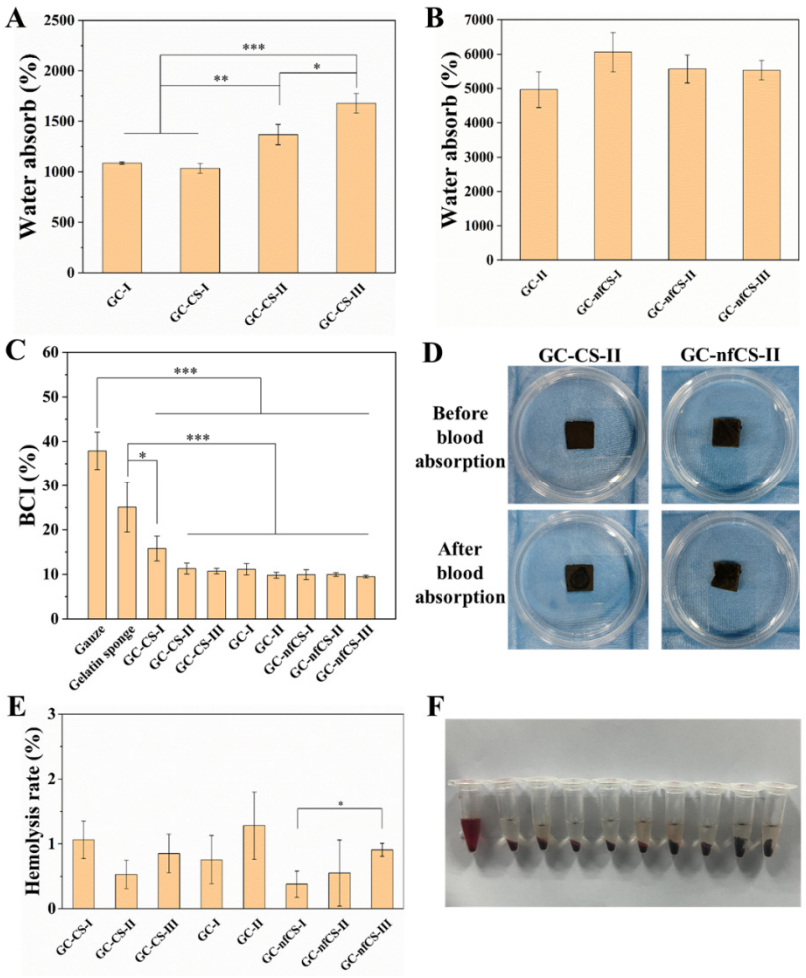

Figure 3. The characterization of GC-CS and GC-nfCS aerogels. The water absorption of (**A**) different GC-CS aerogels and (**B**) different GC-nfCS aerogels. The GC-CS and GC-nfCS aerogels could achieve high mass ratio of absorption liquid within 5 s. (**C**) The BCI of GC-CS and GC-nfCS aerogels. (**D**) The shape change of aerogels before and after blood absorption. The GC-CS aerogels could keep shape very well after absorbing blood. (**E**) The hemolysis rate of GC-CS and GC-nfCS aerogels. The hemolysis rate of GC-CS-II and GC-nfCS-II aerogels was much lower than that of international standard upper limit requirement (5%). (**F**) The photographs of hemolysis assays (From left to right: positive control, negative control, GC-CS-I, GC-CS-II, GC-CS-III, GC-I, GC-II, GC-nfCS-I, GC-nfCS-II and GC-nfCS-III). The GC-CS and GC-nfCS aerogels exhibited good liquid absorption capacity, in vitro blood coagulation and hemolysis capacity. (* $p < 0.05$, ** $p < 0.01$, *** $p < 0.001$)

3.3. Mechanical Properties

Previous studies demonstrated the ordered microstructure could affect the macroscopic mechanical properties of materials [37–39]. Therefore, we further conducted the mechanical test to determine the elasticity of aerogels. A certain elasticity not only could efficiently avoid the damage during package, storage or transportation processes, but also provide convenience for application in narrow or irregular wounds. Firstly, the aerogels were tested at compressive strain from 10% to 50% (Figure 4A). It was found that the GC-CS-II aerogels had no obvious mechanical failure behavior even at compressive strain higher than 40%. Then, the cyclic compression test was further conducted to observe elastic recovery performance at compressive strain of 40% (Figure 4B). The GC-CS-II aerogels still maintained good elastic mechanical properties after 6 cycles of compression test. The maximum compressive strength of GC-CS-II aerogels after 6 cycles could reach over 88% of strength of the first cycle. Therefore, the GC-CS-II aerogels possessed good elastic recovery performance. On the other hand, although the GC-nfCS-II aerogels showed a certain elasticity, their elasticity recovery performance was not as good as GC-CS-II aerogels. As shown in Figure 4C, the compressive strength of GC-nfCS-II aerogels began to attenuate when the compressive strain above 20%. After 6 cycles of compression test, the maximum compressive strength of GC-nfCS-II aerogels only reached 64% of strength of the first cycle (Figure 4D). Moreover, the height of GC-nfCS-II aerogels decreased over 10% after the first compression test. The reduced elasticity of GC-nfCS-II aerogels may due to their large interlayer spacing and little interconnected bridges between lamellar layers.

In order to investigate the influence of orderly microstructure on the mechanical properties, we further prepared aerogels with the same components as GC-CS-II but disordered microstructure (named as GC-CS-II-disorder). The GC-CS-II-disorder aerogels showed obvious mechanical failure at compressive strain of 20% (Figure S8). In addition, the GC-CS-II-disorder aerogels were completely destroyed after the first compression test, indicating no elastic recovery ability of aerogels with disordered microstructure. The above results showed that the ordered channel microstructure was beneficial for improving the elasticity of aerogels.

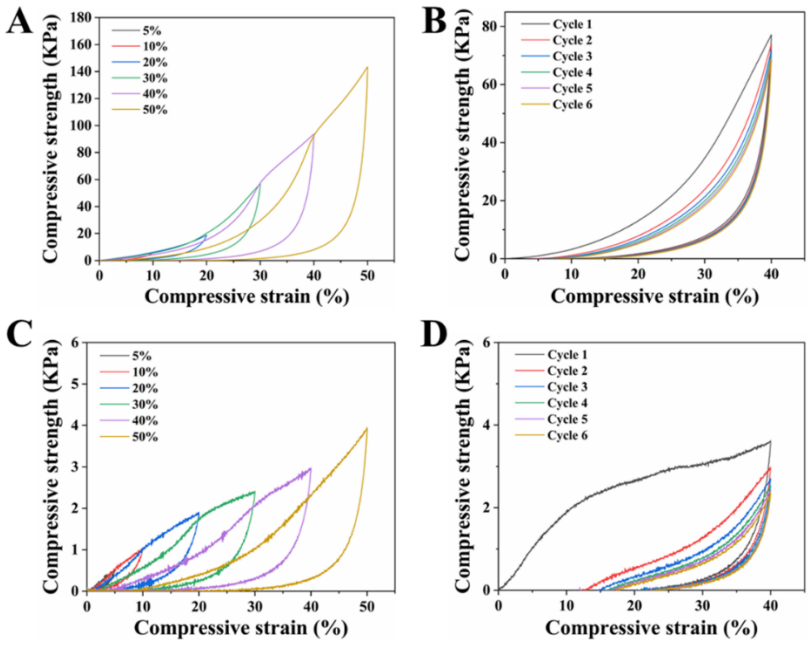

Figure 4. The mechanical performance of GC-CS-II and GC-nfCS-II aerogels. (**A**) Compressive strength and (**B**) cyclic compressive properties of GC-CS-II aerogels. (**C**) Compressive strength and (**D**) cyclic compressive properties of GC-nfCS-II aerogels. The GC-CS-II and GC-nfCS-II aerogels possessed certain elasticity owing to orderly microstructure. Especially, GC-CS-II aerogels showed excellent elastic recovery performance.

3.4. In Vitro Cytocompatibility and In Vivo Hemostasis Performance

The RBCs adhesion on aerogels was further characterized by SEM. There were many echinocytes with numerous thorns besides normal RBCs on gauze and gelatin sponge (Figure 5A). In the GC-nfCS-II group, although few echinocytes were observed, most of RBCs were transferred into spherocytes with spherical shape. On the contrary, RBCs showed normal discal shape rather than abnormal shapes on the GC-CS-II aerogel. Therefore, GC-CS-II aerogel showed little negative effect on physiological status of RBCs, indicating the good cytocompatibility of this aerogel [4]. There are many influence factors for the production of echinocytes, such as the changes of electrolyte concentration, pH value or intracellular calcium [4]. However, the function of echinocytes on hemostasis has not been summarized into an uncontested theory.

Encouraged by superior in vitro hemostatic effect, good cytocompatibility and ultralow hemolysis rate of graphene oxide/chitosan/calcium silicate aerogels, we further investigated in vivo hemostatic effect of aerogels by using rat liver puncture bleeding model. Medical gauze and gelatin sponge were selected as control groups. As shown in Figure 5B–D, owing to the poor blood clotting ability of gauze, there was abundant bleeding in this group. The hemolysis time and blood loss amount of gauze were 150.8 s and 556.7 mg, respectively. The gelatin sponge had better hemostatic performance with hemolysis time of 107.8 s and blood loss amount of 374.6 mg. As for the GC-CS-II and GC-nfCS-II aerogels, they showed significantly enhanced hemostasis effect comparing with gauze and gelatin sponge. The hemostasis times of GC-CS-II and GC-nfCS-II were 80.8 s and 46.3 s, respectively. The blood loss amounts of two graphene oxide/chitosan/calcium silicate aerogels were lower than 280 mg, which were far less than that of gauze and gelatin sponge. Therefore, these two graphene oxide/chitosan/calcium silicate aerogels exhibited excellent in vivo hemostatic function, showing great potential in rapid hemostasis in traumatic wounds.

The hemostasis mechanism of these aerogels was also investigated to fully understand the hemostasis performance. Similar to other hemostatic sponges/aerogels, the two graphene oxide/chitosan/calcium silicate aerogels also could quickly absorb plasma and promote blood cells enrichment due to their porous structure and

rapid liquid absorbing capacity [2]. It was observed that the abundant blood cells were accumulated on the surface of aerogels (Figure 5E), which was benefiting to platelet aggregation and activation during primary hemostasis. In addition, the graphene oxide/chitosan/calcium silicate aerogels had negative zeta potential (Figure 5F). The negatively charged surfaces could activate the expression of coagulation factors XII in intrinsic pathways of secondary hemostasis, which could promote blood clotting [2,40]. Partial thromboplastin time (PTT) was determined to evaluate the effect of materials on intrinsic pathways of hemostasis process (Figures 5G and S9). The PTTs of GC-CS-II and GC-nfCS-II were significantly lower than blank control and negative control, demonstrating that GC-CS-II and GC-nfCS-II could activate the intrinsic pathway of coagulation. Therefore, such graphene oxide/chitosan/calcium silicate aerogels achieved rapid hemostasis through the synergistic effect of different hemostasis pathways.

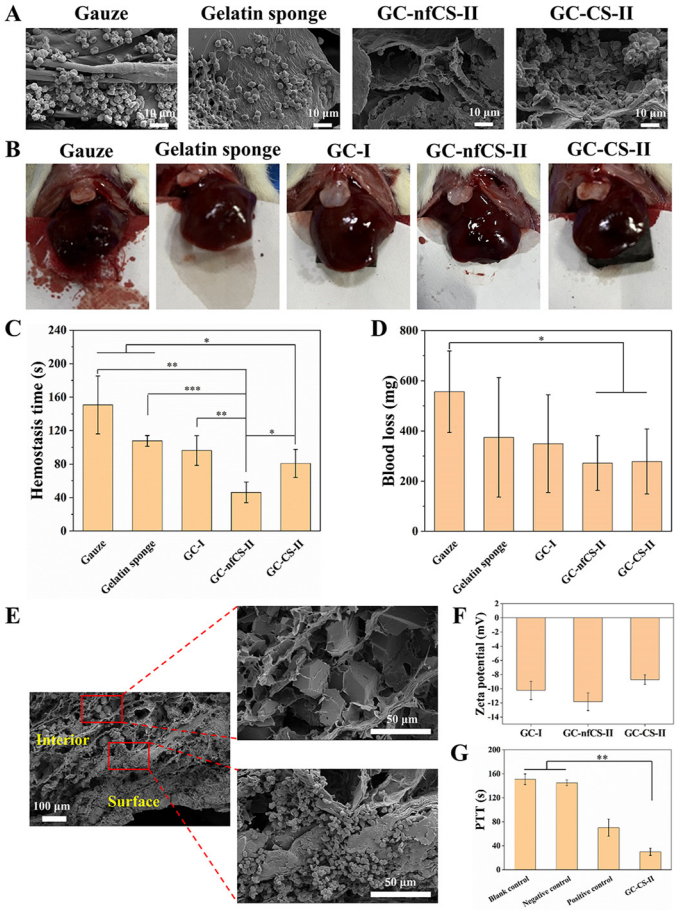

Figure 5. In vitro cytocompatibility and in vivo hemostasis performance of GC-CS-II and GC-nfCS-II aerogels. (**A**) RBCs adhesion of different aerogels. (**B**) Photographs of in vivo hemostasis assays of different groups. (**C**) Hemostasis times and (**D**) blood loss of different aerogels on rat liver puncture bleeding models. The graphene oxide/chitosan/calcium silicate aerogels exhibited good hemostasis performance in vivo. (**E**) The Cross-section morphology of GC-CS-II aerogel after blood coagulation. (**F**) Zeta potential of different aerogels. (**G**) PTT of GC-CS-II aerogel. The graphene oxide/chitosan/calcium silicate aerogels achieved rapid hemostasis through the synergistic effect of different hemostasis pathways, including the promotion of blood cells enrichment and activation of the intrinsic pathway of coagulation. (* $p < 0.05$, ** $p < 0.01$, *** $p < 0.001$)

3.5. In Vivo Infectious Wound Healing Performance

Rapid bleeding is always accompanied with deep or large-area wounds of tissue. Hemostasis is the primary step of wound healing. Besides, the wounds also easily infected under exposure environments. Therefore, the infectious wound model was used to evaluate the in vivo anti-bacteria and wound healing performance of aerogels. Considering the good photothermal effect of GO component, the wounds covered with graphene oxide/chitosan/calcium silicate aerogels were taken with photothermal therapy at the firstly three days. The photothermal temperature in wound sites were kept at approximately 50–56 ℃ for 10 min (Figure 6A,B). On the contrary, the wounds of blank group did not cover with aerogels and was not treated with photothermal therapy.

Besides, considering the poor photothermal performance of gauze and gelatin sponge and animal welfare, we did not set extra groups for gauze and gelatin sponge with photothermal therapy in skin wound healing experiments.

As shown in Figure 6C, the untreated blank group showed obvious inflammation in skin wounds even at day 7, which also affected the healing of wounds. For the GC-I, GC-nfCS-II and GC-CS-II groups, the inflammation in the skin wounds could be significantly inhibited after continuously photothermal therapy for three days. At day 4, there were no inflammation on the wounds in the GC-nfCS-II and GC-CS-II groups, which verified the good anti-bacteria effect of these two aerogels. After 14 days of treatment, the wound closure rate of GC-nfCS-II and GC-CS-II reached above 98.6% and 99.5%, respectively (Figure 6D). HE staining were further conducted to observe the tissue repairing conditions of each group (Figures 7A and S10). At day 14, the wounds in the GC-nfCS-II and GC-CS-II groups almost healed and formed continuous epidermis while Blank group had not formed complete epidermis layer. Moreover, the GC-nfCS-II and GC-CS-II groups also showed more complete skin tissue structure than the GC-I group, including epidermis and dermis.

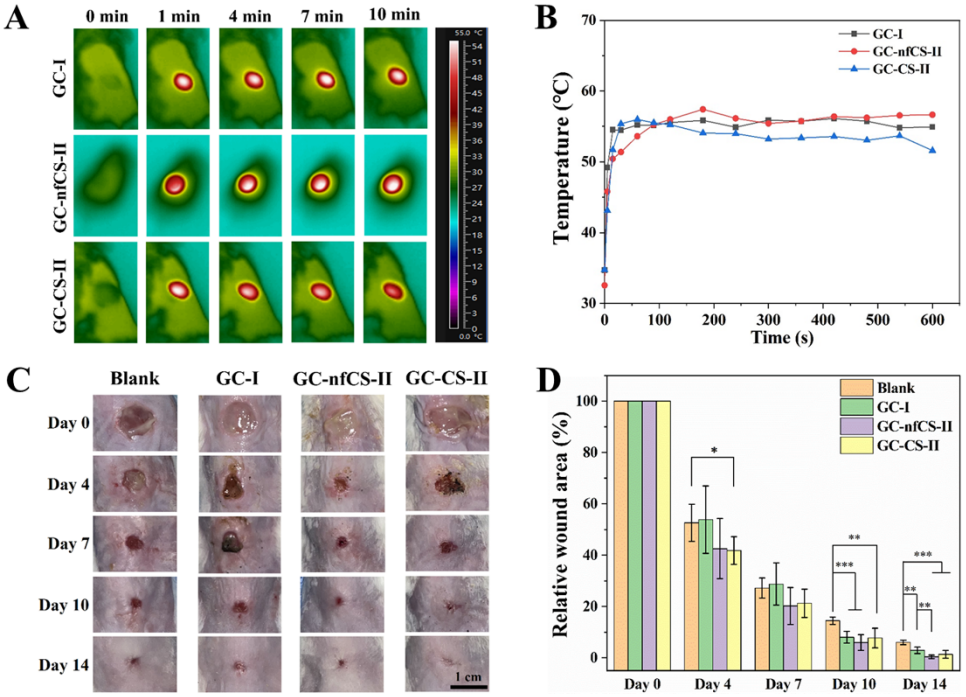

Figure 6. In vivo infectious wound healing performance of GC-CS-II and GC-nfCS-II aerogels. (**A**) Infrared thermal images and (**B**) temperature curves of infectious skin wounds under photothermal therapy. (**C**) Photographs and (**D**) relative wound area of infectious skin wounds with time in different groups. The infectious conditions of wounds were significantly inhibited after photothermal therapy in GC-CS-II and GC-nfCS-II groups. The skin wounds treated with GC-CS-II and GC-nfCS-II aerogels showed better wound healing rate than Blank group. (* $p < 0.05$, ** $p < 0.01$, *** $p < 0.001$)

The collagen fibers in dermis of each group were also investigated by Masson staining. The aniline blue used in Masson staining could be immersed in the structural loose and highly permeable collagen fibers, so the collagen fibers appeared blue color after Masson staining. There were little collagen fibers in the wound site of Blank group. The distribution area of collagen in the GC-nfCS-II and GC-CS-II groups was larger than other two groups (Figure 7B). In the early stage of wound healing, the photothermal therapy in the first three days of three graphene oxide/chitosan/calcium silicate aerogel groups significantly suppressed the infectious inflammation at wounds. Moreover, previous studies demonstrated that Si ions could favor the proliferation of endothelial cells and fibroblasts and promote the healing of diabetic skin wounds [32,41]. Therefore, it is reasonable to speculate that Si ions in GC-nfCS-II and GC-CS-II aerogels were beneficial to the healing quality of skin wounds. Taken together, GC-nfCS-II and GC-CS-II aerogels had better wound healing rate and quality for infectious skin wounds.

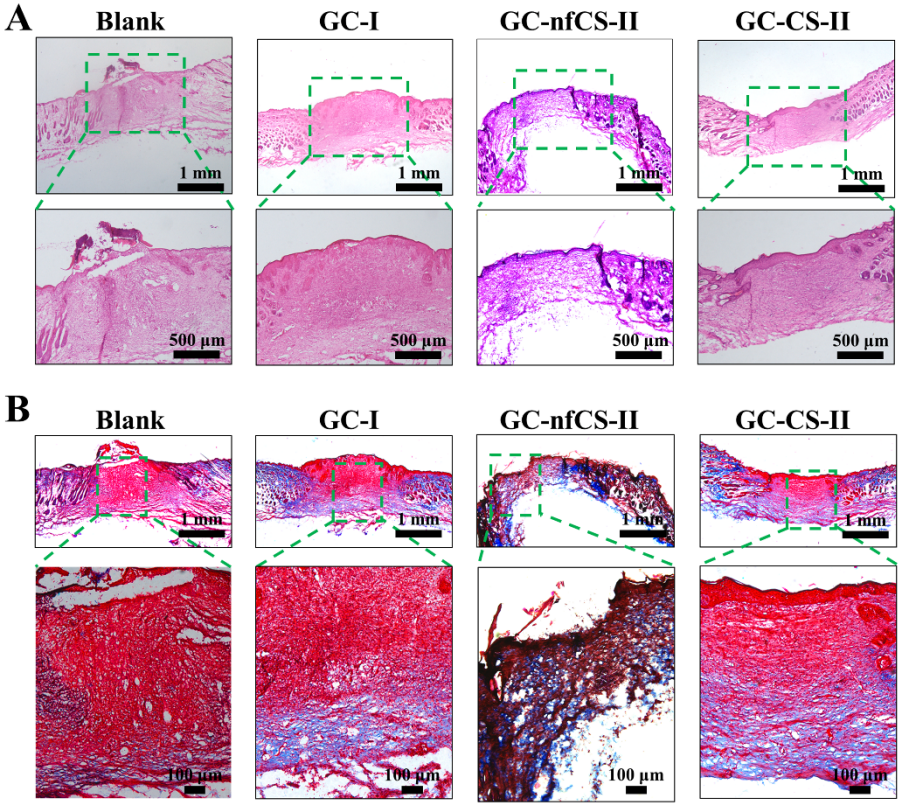

Figure 7. Histological analysis of skin tissue at wound sites after treated with GC-CS-II and GC-nfCS-II aerogels. (**A**) HE staining images and (**B**) Masson staining images of different groups for 14 days. The GC-nfCS-II and GC-CS-II aerogels exhibited better wound healing quality for infectious skin wounds comparing with Blank groups.

4. Conclusions

In summary, two types of multifunctional graphene oxide/chitosan/calcium silicate aerogels (i.e., GC-CS-II and GC-nfCS-II) were successfully fabricated. The GC-CS-II and GC-nfCS-II aerogels showed oriented porous microstructure with interconnected channels, which also lead to the high liquid absorption capacity within 5 s. Although the liquid absorption capacity of GC-nfCS-II aerogels was much higher than that of GC-CS-II aerogels, it should be noticed that high porosity and large interlayer spacing between channels of GC-nfCS-II aerogels reduced their elasticity and shape retention ability in the wet state. Therefore, the balancing between high porosity and good mechanical performance should be considered in future hemostasis aerogels/sponges design. More importantly, compared with gauze and gelatin sponge, the GC-nfCS-II and GC-CS-II aerogels could achieve rapid hemostasis of liver puncture bleeding and less blood loss amount. In addition, these two aerogels could significantly inhibit bacteria and accelerate the healing process of infectious skin wounds. These graphene oxide/chitosan/calcium silicate aerogels with good hemostasis, anti-bacteria and wound healing abilities have great potential in treatment of emergency trauma.

Supplementary Materials

The additional data and information can be downloaded at: https://media.sciltp.com/articles/others/2506171401300756/RMD-1007-Supporting-Materials-Final.pdf. Figure S1: The morphology of calcium silicate hydrate nanofibers; Figure S2: The XRD pattern of calcium silicate hydrate nanofibers; Figure S3: The EDS mapping of different GC-CS aerogels; Figure S4: The EDS mapping of different GC-CS aerogels; Figure S5: The XRD and FTIR of different materials; Figure S6: The photographs of different groups after BCI tests; Figure S7: The in vitro photothermal performance of different materials; Figure S8: The compressive properties of GC-CS-II-disorder aerogel; Figure S9: PTT of GC-CS-II aerogel; Figure S10: HE staining images of different groups for 7 days; Table S1: The constituent contents of different aerogels.

Author Contributions

J.X.: Conceptualization, Investigation, Methodology, Data analysis, Validation, Writing–original draft; Y.Z. (Yi Zheng): Conceptualization, Investigation, Methodology, Data analysis, Validation; Z.Y.: Investigation, Methodology, Data analysis; J.H.: Investigation, Methodology, Data analysis; W.M.: Investigation; Z.H.:

Resources, Project administration, Funding acquisition; Y.Z. (Yufang Zhu).: Conceptualization, Supervision, Project administration, Writing—review & editing, Funding acquisition; C.W.: Conceptualization, Supervision, Project administration, Writing—review & editing, Funding acquisition. All authors have read and agreed to the published version of the manuscript.

Funding

This work was supported by the National key Research and Development Program of China (2023YFB3813000), the National Natural Science Foundation of China (32225028), Joint Research Unit Plan of Chinese Academy of Sciences (121631ZYLH20240014), and Science and Technology Commission of Shanghai municipality (24520750100).

Institutional Review Board Statement

All procedures of animal experiments were approved by the Institutional Animal Care and Use Committee of Nanjing First Hospital, Nanjing Medical University (DWSY-2102163).

Data Availability Statement

The data in the current study is available from the corresponding author on reasonable request.

Conflicts of Interest

The authors declare that they have no competing interests.

References

1. Guo, B.; Dong, R.; Bang, Y.; et al. Haemostatic materials for wound healing applications. *Nat. Rev. Chem.* **2021**, *5*, 773–791.
2. Dong, R.; Zhang, H.; Guo, B. Emerging hemostatic materials for non-compressible hemorrhage control. *Natl. Sci. Rev.* **2022**, *9*, nwac162.
3. Zheng, Y.; Ma, W.; Yang, Z.; et al. An ultralong hydroxyapatite nanowire aerogel for rapid hemostasis and wound healing. *Chem. Eng. J.* **2022**, *430*, 132912.
4. Jimenez-Martin, J.; Heras, K.L.; Etxabide, A.; et al. Green hemostatic sponge-like scaffold composed of soy protein and chitin for the treatment of epistaxis. *Mater. Today Bio* **2022**, *15*, 100273.
5. Fang, Y.; Xu, Y.; Wang, Z.; et al. 3D porous chitin sponge with high absorbency, rapid shape recovery, and excellent antibacterial activities for noncompressible wound. *Chem. Eng. J.* **2020**, *388*, 124169.
6. Li, G.; Quan, K.; Liang, Y.; et al. Graphene-Montmorillonite Composite Sponge for Safe and Effective Hemostasis. *ACS Appl. Mater. Interfaces* **2016**, *8*, 35071–35080.
7. Jiang, T.; Chen, S.; Xu, J.; et al. Superporous sponge prepared by secondary network compaction with enhanced permeability and mechanical properties for non-compressible hemostasis in pigs. *Nat. Commun.* **2024**, *15*, 5460.
8. Wan, W.; Feng, Y.; Tan, J.; et al. Carbonized Cellulose Aerogel Derived from Waste Pomelo Peel for Rapid Hemostasis of Trauma-Induced Bleeding. *Adv. Sci.* **2024**, *11*, 2307409.
9. Zheng, L.; Li, X.; Xu, C.; et al. High-Efficiency Antibacterial Hemostatic AgNP@Zeolite/Chitin/Bamboo Composite Sponge for Wound Healing without Heat Injury. *Adv. Healthc. Mater.* **2023**, *12*, 2300075.
10. He, G.; Xian, Y.; Lin, H.; et al. An injectable and coagulation-independent Tetra-PEG hydrogel bioadhesive for post-extraction hemostasis and alveolar bone regeneration. *Bioact. Mater.* **2024**, *37*, 106–118.
11. Ye, R.; Zhu, Z.; Gu, T.; et al. Neutrophil extracellular traps-inspired DNA hydrogel for wound hemostatic adjuvant. *Nat. Commun.* **2024**, *15*, 5557.
12. Zhao, X.; Huang, Y.; Li, Z.; et al. Injectable Self-Expanding/Self-Propelling Hydrogel Adhesive with Procoagulant Activity and Rapid Gelation for Lethal Massive Hemorrhage Management. *Adv. Mater.* **2024**, *36*, 202308701.
13. Fan, P.; Dong, Q.; Yang, J.; et al. Flexible dual-functionalized hyaluronic acid hydrogel adhesives formed in situ for rapid hemostasis. *Carbohydr. Polym.* **2023**, *313*, 120854.
14. Pourshahrestani, S.; Kadri, N.A.; Zeimaran, E.; et al. Well-ordered mesoporous silica and bioactive glasses: promise for improved hemostasis. *Biomater. Sci.* **2019**, *7*, 31–50.
15. Tong, L.; Zhang, D.; Huang, Z.; et al. Calcium Ion-Coupled Polyphosphates with Different Degrees of Polymerization for Bleeding Control. *ACS Appl. Mater. Interfaces* **2024**, *16*, 43244–43256.
16. Su, C.; Jiang, C.; Sun, X.; et al. Diatomite hemostatic particles with hierarchical porous structure for rapid and effective hemostasis. *Colloids Surf. B* **2022**, *219*, 112809.

17. Li, Q.; Hu, E.; Yu, K.; et al. Self-Propelling Janus Particles for Hemostasis in Perforating and Irregular Wounds with Massive Hemorrhage. *Adv. Funct. Mater.* **2020**, *30*, 2004153.
18. Lu, X.; Li, X.; Yu, J.; et al. Nanofibrous hemostatic materials: Structural design, fabrication methods, and hemostatic mechanisms. *Acta Biomater.* **2022**, *220*, 112891.
19. Wang, A.; Du, F.; He, Y.; et al. Graphene oxide reinforced hemostasis of gelatin sponge in noncompressible hemorrhage via synergistic effects. *Colloids Surf. B* **2022**, *220*, 112891.
20. Sun, Z.; Hu, K.; Wang, T.; et al. Enhanced physiochemical, antibacterial, and hemostatic performance of collagen-quaternized chitosan-graphene oxide sponges for promoting infectious wound healing. *Int. J. Biol. Macromol.* **2024**, *266*, 131277.
21. Li, S.; Gu, B.; Li, X.; et al. MXene-Enhanced Chitin Composite Sponges with Antibacterial and Hemostatic Activity for Wound Healing. *Adv. Healthc. Mater.* **2022**, *11*, 2102367.
22. Yang, F.; Jia, X.; Hua, C.; et al. Highly efficient semiconductor modules making controllable parallel microchannels for non-compressible hemorrhages. *Bioact. Mater.* **2024**, *36*, 30–47.
23. Khosravi, Z.; Kharaziha, M.; Goli, R.; et al. Antibacterial adhesive based on oxidized tannic acid-chitosan for rapid hemostasis. *Carbohydr. Polym.* **2024**, *333*, 121973.
24. Zheng, Y.; Xue, J.; Ma, B.; et al. Mesoporous Bioactive Glass-Graphene Oxide Composite Aerogel with Effective Hemostatic and Antibacterial Activities. *ACS Appl. Bio Mater.* **2024**, *7*, 429–442.
25. Sridhar, S.K.; Goudanavar, P.; Rao GS, N.K.; et al. Innovations in nano-enhanced healing: Patent insights and clinical trials on nanotubes in wound recovery. *Mater. Today Commun.* **2024**, *41*, 110750.
26. Chao, Y.; Yu, S.; Zhang, H.; et al. Architecting Lignin/Poly(vinyl alcohol) Hydrogel with Carbon Nanotubes for Photothermal Antibacterial Therapy. *ACS Appl. Bio Mater.* **2023**, *6*, 1525–1535.
27. Zheng, Y.; Wu, J.F.; Zhu, Y.F.; et al. Inorganic-based biomaterials for rapid hemostasis and wound healing. *Chem. Sci.* **2022**, *14*, 29–53.
28. Fan, S.; Wu, X.; Fang, Z.; et al. Injectable and ultra-compressible shape-memory mushroom: Highly aligned microtubules for ultra-fast blood absorption and hemostasis. *Chem. Eng. J.* **2023**, *460*, 140554.
29. Wang, L.; Zhong, Y.; Qian, C.; et al. A natural polymer-based porous sponge with capillary-mimicking microchannels for rapid hemostasis. *Acta Biomater.* **2020**, *114*, 193–205.
30. Ong, S.Y.; Wu, J.; Moochhala, S.M.; et al. Development of a chitosan-based wound dressing with improved hemostatic and antimicrobial properties. *Biomaterials* **2008**, *29*, 4323–4332.
31. Zhou, Y.; Wu, C.; Chang, J. Bioceramics to regulate stem cells and their microenvironment for tissue regeneration. *Mater. Today* **2019**, *24*, 41–56.
32. Lv, F.; Wang, J.; Xu, P.; et al. A conducive bioceramic/polymer composite biomaterial for diabetic wound healing. *Acta Biomater.* **2017**, *60*, 128–143.
33. Chen, K.; Tang, X.K.; Yue, Y.H.; et al. Strong and tough layered nanocomposites with buried interfaces. *ACS Nano* **2016**, *10*, 4816–4827.
34. Xue, J.; Wang, X.; Wang, E.; et al. Bioinspired multifunctional biomaterials with hierarchical microstructure for wound dressing. *Acta Biomater.* **2019**, *100*, 270–279.
35. Wang, Y.; Li, J.; Li, X.; et al. Graphene-based nanomaterials for cancer therapy and anti-infections. *Bioact. Mater.* **2022**, *14*, 335–349.
36. Huang, C.; Chen, L.; Liu, X.; et al. Effect of tranexamic acid-functionalized photothermal hydrothermal treated oxidized graphene sponge on diabetic wound healing: Hemostasis, antibacterial, and regeneration. *Mater. Design* **2025**, *253*, 113915.
37. Nepal, D.; Kang, S.; Adstedt, K.M.; et al. Hierarchically structured bioinspired nanocomposites. *Nat. Mater.* **2023**, *22*, 18–35.
38. Wegst, U.G.; Bai, H.; Saiz, E.; et al. Bioinspired structural materials. *Nat. Mater.* **2015**, *14*, 23–36.
39. Yang, M.; Zhao, N.; Cui, Y.; et al. Biomimetic Architectured Graphene Aerogel with Exceptional Strength and Resilience. *ACS Nano* **2017**, *11*, 6817–6824.
40. Feng, Y.; Luo, X.; Wu, F.; et al. Systematic studies on blood coagulation mechanisms of halloysite nanotubes-coated PET dressing as superior topical hemostatic agent. *Chem. Eng. J.* **2022**, *428*, 132049.
41. Li, H.; Chang, J. Stimulation of proangiogenesis by calcium silicate bioactive ceramic. *Acta Biomater.* **2013**, *9*, 5379–5389.